

Preparation, morphology, crystal structure, energy gap and photoluminescence studies of Mn²⁺/Cr³⁺ doped ZnS quantum dots

P.J. Binu

PG & Research Department of Physics, Government Arts College

S. Muthukumar (✉ drsmk123@yahoo.co.in)

PG & Research Department of Physics, Government Arts College <https://orcid.org/0000-0002-6050-0782>

Research Article

Keywords: Cr/Mn dual doped ZnS, Crystallite size, Energy gap, FTIR, Photoluminescence, Defects

Posted Date: May 28th, 2021

DOI: <https://doi.org/10.21203/rs.3.rs-563619/v1>

License: © ⓘ This work is licensed under a Creative Commons Attribution 4.0 International License.

[Read Full License](#)

Abstract

Mn added ZnS ($\text{Zn}_{0.97}\text{Mn}_{0.03}\text{S}$) and Mn-Cr doped ZnS ($\text{Zn}_{0.95}\text{Mn}_{0.03}\text{Cr}_{0.02}\text{S}$) nanostructures were synthesized by co-precipitation process. X-ray diffraction analysis confirmed the cubic phase with highest intensity along (111) orientation. The shrinkage of crystallite size from 36 Å ($\text{Zn}_{0.97}\text{Mn}_{0.03}\text{S}$) to 26 Å ($\text{Zn}_{0.95}\text{Mn}_{0.03}\text{Cr}_{0.02}\text{S}$) and the influence of Cr and Mn on morphology, optical and photoluminescence characters in ZnS were investigated. The substitution of Cr in Zn-Mn-S lattice not only diminished the crystallite size and also produced more defect associated luminescent activation centres. The presence of Zn^{2+} , Mn^{2+} and Cr^{3+} ions in Zn-Mn-Cr-S lattice was confirmed by XPS spectra. The elevation in energy gap by Cr addition was explained by Burstein–Moss effect and reduced crystallite size. The tuning of energy gap as well crystallite size of basic ZnS nanostructure by Mn/Cr substitution encourages these materials for modern electronic applications. FTIR spectra established the occurrence of Mn/Cr in Zn-S lattice by their characteristic bondings. The inclusion of Mn /Cr provides an efficient control over modification of various emissions which suggests their applications in organic light emitting diode materials.

1. Introduction

Recently, group II-VI semiconducting materials exhibit great scientific and technological significance within different family of semiconductors because of their numerous practical applications in science and technology [1–4]. Quantum dots (QDs) are semiconducting material of nano-scale dimensions with distinctive properties determined by its size. Yang et al. [5] investigated N and S heavily doped carbon quantum dot (CQDs) with size around 1–6 nm which had better photoluminescence (PL) behaviour and better sensitive to Cu^{2+} and Hg^{2+} , respectively. Selenium added graphene QDs [6] with size around 1–5 nm possessed a quantum field of 0.29 and a PL lifetime of 3.44 ns which guaranteed a better selectivity for the fluorescent switch. Wang et al. [7] reported the controlled PL behaviour in sulfur doped GQDs by tuning the S concentrations. Huang and their co-workers [8] developed a weak electrolyte-based electrochemical method to enhance the oxidation and cutting process and achieved a better yield of GQDs.

Porous based graphene (PGN) showed an outstanding performance in PGN based detectable molecule separation or other biomedical applications [9]. Zhu and their co-workers [10] demonstrated that graphene oxide can be oxidized and cut into GQDs by hydroxyl radicals. Back-gated field-effect transistors made of single-layer C_3N exhibited an on–off current ratio reaching 5.5×10^{10} [11]. The challenges of developing solid-state PL CQDs induced a great curiosity among research people [12]. Nitrogen based CD probes can also distinguish tumor cells from normal cells and be used to evaluate their proliferation activity [13].

Among the different semiconducting materials, ZnS is the significant one due to its unique properties [14] and applications [15–17]. The two most common forms of ZnS are zinc blende and wurtzite structure where the energy gap varied between 3.72–3.77 eV [18–19]. Moreover, ZnS have the elevated

transmittance in the higher wavelength and significantly huge exciton binding energy and so helpful for manipulating well-organized optoelectronic device applications [20–22]. By its unique features and characteristics, ZnS can be employed in an extensive spectrum of different applications like solar cells, photo-voltaics, sensors, electroluminescence devices, modern emitting diodes, and lasers [23, 24].

The intentional doping of metal ions into ZnS is fundamental to modify the optical nature of semiconducting materials by building innovative quantum states between two bands of semiconductors [25, 26]. ZnS is believed as a suitable host material for optically dynamic elements like transition metal (TM) ions, which can fascinatingly provoke a impressive changes in energy level structures, surface activities, visual and electrical characteristics and stimulates its transition probabilities [27–29]. In optoelectronic applications, it is essential that the doping element enclose a deep energy level and elevated voltage stability. Therefore, TM ions can be chosen as a suitable element due to the extraordinary properties accessible by an inclusion into ZnS basic lattice [29, 30].

The modified and improved property of ZnS by the addition of TM element has created an immense curiosity in the possibility to alter and elevate their optical and micro-structural properties for their scientific and industrial applications [31]. Among the various possible TM ions, manganese (Mn^{2+}) is considered as one of the best and significant doping agents owing to its extraordinary luminescence characters using in optical sensors, phosphors, lasers, fluorescence bio-imaging and displays [3, 33]. The ionic radius and the ionic charge of Mn^{2+} ion is realistically close to Zn^{2+} ion. Moreover, Mn^{2+} occupies the various sites of ZnS lattice and stimulates the considerable modification in its optical, structural, microstructure, electronic properties [34–36]. Up to now, an immense deal of hard work has been paid to inspect the optical nature and structure of Mn doped ZnS semiconducting material due to its excellent thermal and photo-stability.

Bhargava et al. [37] achieved the superior quantum efficiencies and better lifetime shortening by Mn in ZnS lattice. Kripal [38] studied the luminescence and conductivity nature of Mn substituted ZnS nanostructures and they noticed that the photo-sensitivity was enhanced by Mn^{2+} into ZnS system. A noticeable increase in visible transmittance and a small decline in resistivity by Mn^{2+} in ZnS were found by Jrad [39]. Goudarzi et al. [40] described that the insertion of Mn occupied the substitutional position of Zn and modified the energy level of ZnS which promotes the elevated luminescence properties. The luminescence and photo-catalytic studies carried out by Nasser [41] in Mn / ZnS described that the inclusion of Mn^{2+} stimulates the charge separation and activate the photo-catalytic activity of Mn doped ZnS. From the literature it is understood that the higher percentage of Mn produced the secondary phase generation. To avoid the secondary phase generation, Mn level is optimized as 3% ($Zn_{0.97}Mn_{0.3}S$).

The adding of two or more elements through ZnS causes a significant progression in photoluminescence, energy gap, size and charge transport properties. Doping at higher percentage with no secondary phase or metallic cluster is achieved by the adding two or more suitable TM ions [42]. In this work, Cr is chosen as second doping element because it can easily enters into ZnS lattice [43] and enhanced the stability of ZnS [44]. The higher doping percentage without secondary phase is achieved by Cr doping. The Cr

percentage is limited to 2% and it is attained by fixing the appropriate of quantity of precursors. Moreover, the addition of Cr^{3+} through ZnS stimulates the different special defect sites in the lattice owing to the dissimilarities among Cr^{3+} and Zn^{2+} ions. Poornaprakash reported the disappearance of blue emission bands and appearance of RTFM by Cr addition in ZnS [45]. Recently, Aqeel et al. [46] described that Cr added ZnS performed the superior photocatalytic behaviour and hence they may use as an effective one for the elimination of environmental pollutants.

Lattice contraction and the enhancement of energy levels were reported by Reddy et al. [47] in ZnS with increase of Cr concentrations. Yang et al. [48] noticed the strong higher wavelength emissions within 515–560 nm in Co^{2+} , Cu^{2+} dual doped ZnS nanostructure. The PL intensity of dual doped material is considerably superior than ZnS. Liu et al. [49] reported the red radiation emission in Mn-Cd dual doped ZnS nanostructures. Yang et al. [50] described the PL characteristics of Ni^{2+} / Mn^{2+} doped ZnS. The similar PL studies were made on Mn, Pr co-doped ZnS [51], Co-Cu doped ZnS [52], Cu-Mn doped ZnS nanostructures [53].

The optical, structural, PL and magnetic studies on Mn single doped ZnS [31–41], Cr single added ZnS [43–47] and some other TM dual doped ZnS [48–53] were reported in the literature. But, the comprehensive investigation of optical, morphological and emission characters on Cr, Mn dual doped ZnS is almost scanty. In this work, $\text{Zn}_{0.97}\text{Mn}_{0.03}\text{S}$ and $\text{Zn}_{0.95}\text{Mn}_{0.03}\text{Cr}_{0.02}\text{S}$ quantum dots (QDs) were synthesized by co-precipitation route. The structural, spectral, morphological and PL properties of the $\text{Mn}^{2+}/\text{Cr}^{3+}$ doped ZnS QDs are characterized systematically to achieve the better insight about the crystal nature, morphology, bonding nature, energy gap and emission properties.

2. Experimental Details

2.1. Preparation of $\text{Zn}_{0.97}\text{Mn}_{0.03}\text{S}$ and $\text{Zn}_{0.95}\text{Mn}_{0.03}\text{Cr}_{0.02}\text{S}$ QDs

The preparation of $\text{Zn}_{0.97}\text{Mn}_{0.03}\text{S}$ and $\text{Zn}_{0.95}\text{Mn}_{0.03}\text{Cr}_{0.02}\text{S}$ QDs has been carried out by co-precipitation route. Zinc acetate ($\text{Zn}(\text{CH}_3\text{COO})_2 \cdot 2\text{H}_2\text{O}$), Na_2S , manganese acetate ($\text{Mn}(\text{CH}_3\text{COO})_2 \cdot 2\text{H}_2\text{O}$) and chromium acetate dihydrate ($\text{Cr}(\text{CH}_3\text{COO})_2 \cdot 2\text{H}_2\text{O}$) are employed as resource materials for Zn^{2+} , S^{2-} , Mn^{2+} and Cr^{3+} ions, respectively. The ultra-pure de-ionized water used as solvent. All the chemicals were bought from M/S. Merck and utilized with no additional purification since they possessed analytical grade (AR) with 99.99% purity. The molar quantities were taken as per the targeted doping concentration i.e. the doping composition of Mn^{2+} is fixed as 3% and Cr^{3+} fixed as 2% to prepare $\text{Zn}_{0.95}\text{Mn}_{0.03}\text{Cr}_{0.02}\text{S}$ QDs. The source materials were weighed as per the expected compositions and dissolved in 100 ml ultra-pure de-ionized water. Separate solutions of manganese acetate, chromium chloride, zinc acetate and Na_2S were prepared.

For the synthesis of $\text{Zn}_{0.95}\text{Mn}_{0.03}\text{Cr}_{0.02}\text{S}$ QDs, 0.95 M $\text{Zn}(\text{CH}_3\text{COO})_2 \cdot 2\text{H}_2\text{O}$ and 0.03 M $\text{Zn}(\text{CH}_3\text{COO})_2 \cdot 2\text{H}_2\text{O}$ were slowly dissolved one by one in 100 ml water under constant stirring to obtain clear and homogeneous solution. After getting homogeneous solution, 0.02 M chromium acetate dihydrate was mixed at constant stirring. A separate solution made by mixing 1M sodium sulfide in 100 ml water is dissolved with the previous solution. The solution was mixed drop wise to the initial solution under constant stirring of 1000 rpm for 8 h at 60°C as in Fig. 1. The preparation process is depending on the slow release of Zn^{2+} , Mn^{2+} , Cr^{3+} and S^{2-} ions in the final solution. The ions condense on an ion-ion basis in the solution. Aqueous ammonia solution was mixed to keep the pH of the mixer solution as 9. After 8 h, a light greenish white precipitate was deposited at the bottom portion of the flask. A wet precipitate was filtered out separately and washed with de-ionized water and methanol to eliminate the undesired impurities. The resultant product was dehydrated by keeping it into a furnace at 60°C for 7 h.

2.2. Characterization techniques

A powder X-ray diffractometer (XRD) was used to explore crystal structure of $\text{Zn}_{0.97}\text{Mn}_{0.03}\text{S}$ and $\text{Zn}_{0.95}\text{Mn}_{0.03}\text{Cr}_{0.02}\text{S}$ QDs. The diffracted patterns were recorded by RigakuC/max-2500 diffractometer using CuK α radiation ($\lambda = 1.5406 \text{ \AA}$) at 40 kV and 30 mA from $2\theta = 20^\circ$ to 70° . The morphology of the prepared QDs were recorded using transmission electron microscopy (Philips- CM200) in the range of operating voltage as 20-200kV. The efficiency of the doping ions in the ZnS was verified by X-ray photoelectron spectroscopy (XPS). The presence of the metal elements was confirmed using XPS spectra (Perkin-Elmer PHI 1600 ESCA) with a monochromatic Mg K α X-ray source ($h\nu = 1486.6 \text{ eV}$) using manual point control object with a scanning rate of 0.5 eV.

The UV-visible optical absorption studies were made to examine their optical properties using UV-visible spectrometer (Model: lambda 35, Make: Perkin Elmer) from 310 nm to 550 nm at ambient temperature. The FTIR studies were done by Fourier transform infra-red (FTIR) spectrometer (Model: Perkin Elmer, Make: Spectrum RX I) from 400 cm^{-1} to 4000 cm^{-1} . Pellets were made by mixing the nanoparticles with KBr at 1 wt%. Room-temperature photoluminescence (PL) studies were made (Model: Hitachi, Make: F-2500) at excitation wavelength of 330 nm and power of 150 W from 345 nm to 700 nm to study the radiative recombination properties.

3. Results And Discussion

3.1. XRD - Structural analysis

Figure 2 represents a typical XRD pattern of $\text{Zn}_{0.97}\text{Mn}_{0.03}\text{S}$ and $\text{Zn}_{0.95}\text{Mn}_{0.03}\text{Cr}_{0.02}\text{S}$ QDs. The obtained XRD patterns exhibit three strong and wide peaks which reflect the nano-crystalline nature of the material [54]. It has been noticed from Fig. 2 that the orientation along (111) plane is preferred one than the orientations such as (220) and (311) because of its high intensity. The obtained major XRD peaks matched well with the JCPDS card No. 80 - 0020 with lattice parameter $a \approx 0.5311 \text{ \AA}$. The well broadened XRD peaks clearly showed the cubic structure of the sample.

The absence of secondary or other impurity phases associated to Cr / Mn metals or its oxides confirmed that both Mn^{2+} and Cr^{3+} ions are properly substituted into the ZnS lattice. No peaks corresponding to strange elements or impurities found in Fig. 2 verified the phase purity of the synthesized samples and also confirmed that the substitution of Mn^{2+} and Cr^{3+} in Zn-S lattice not changed the original cubic structure of the material. Table 1 presents the values of peak intensity, peak position (2θ), full width at half maximum (FWHM, β) value, d- value, lattice parameter 'a', crystallite size (D) and micro strain (ϵ) along (111) plane of $Zn_{0.97}Mn_{0.03}S$ and $Zn_{0.95}Mn_{0.03}Cr_{0.02}S$ nanostructures.

The increase of FWHM along (111) orientation by the addition of Cr indicates the shrinkage of size (Table 1). The peak position along (111) plane of $Zn_{0.97}Mn_{0.03}S$ QDs is shifted to smaller 2θ side by the inclusion of Cr in the Zn-Mn-S lattice. But, Kaur et al. [55] reported that the peak shift is along higher 2θ side by Cr addition in ZnS nanostructure. The peak position shift along smaller 2θ side by Cr addition may possibly owing to the dissimilarity among the ionic radii between Cr, Zn, and Mn ions [56]. The size of the QDs are estimated by Scherrer relation [57],

$$\text{Crystallite size (D)} = 0.9\lambda / (\beta \cos \theta) \quad (1)$$

here, λ is the X-wavelength used, β is the angular peak width at half maximum along (111) plane and θ is the Bragg's diffraction angle. Similarly, the Micro strain (ϵ) provoked in the Zn-Mn-Cr-S lattice is calculated with the help of the relation [58],

$$\text{Micro-strain } (\epsilon) = (\beta \cos \theta) / 4 \quad (2)$$

The derived crystallite size from the Debye relation (seen from Table 1) is diminished from 36 Å ($Zn_{0.97}Mn_{0.03}S$) to 26 Å ($Zn_{0.95}Mn_{0.03}Cr_{0.02}S$) by the inclusion of tiny quantity of Cr (Cr = 2%). The elevated FWHM by Cr doping supports the present shrinkage of size. The value of micro-strain obtained from the above relation is increased from 9.71×10^{-3} ($Zn_{0.97}Mn_{0.03}S$) to 13.11×10^{-3} ($Zn_{0.95}Mn_{0.03}Cr_{0.02}S$). The current enhancement in micro-strain by Cr substitution is also responsible for the decrease of size and the higher micro-strain at Cr = 2% is due to the drop off of activation energy which is originated from higher electro-negativity of Cr ions than Zn^{2+} ions [59]. The drop off of the activation energy and the enhanced micro strain [60] by the Cr inclusion in Zn-Mn-Cr-S lattice deteriorate the crystal and hence suppress the crystal size.

In general, the alteration in lattice constants and inter-planar distance depends upon the nature of dopants and its concentrations, the defect states and strain / stress induced by the dopant in the host lattice and the variation in ionic radii between the dopant and Zn^{2+} [61]. The lattice parameter 'a' is attained by the relation,

$$d_{hkl} = [(h^2 + k^2 + l^2)/a^2]^{-1/2} \quad (3)$$

here, d is lattice spacing, h, k, l are miller indices. Figure 3 shows the alteration in lattice parameter ' a ' and crystallite size for $Zn_{0.97}Mn_{0.03}S$ and $Zn_{0.95}Mn_{0.03}Cr_{0.02}S$ QDs. Both the lattice parameter ' a ' and inter-planner distance ' d ' are increased by Cr incorporation in Zn-Mn-S lattice. Generally, two forms of Cr ions are possible, first one is Cr^{3+} ion which has ionic radius of $\approx 0.63 \text{ \AA}$ and the second one is Cr^{2+} ion which possesses the ionic radius of $\approx 0.89 \text{ \AA}$. The noticed increment in lattice parameters as shown in Table 1 and Fig. 3 may be due to the coexistence of both Cr^{3+} ions and Cr^{2+} ions where the existence of Cr^{2+} ions is higher than Cr^{3+} ions and substitute Zn^{2+} basic ions with the ionic radius of 0.74 \AA in the Zn-Mn-S host lattice [62].

3.2. TEM - Morphological study

TEM micrographs have been taken to get the better understanding about the grain size and shape of the particles. The typical TEM images of $Zn_{0.97}Mn_{0.03}S$ and Cr-doped $Zn_{0.97}Mn_{0.03}S$ QDs are listed in Fig. 4. Figure 4a displays the micro-structural image of $Zn_{0.97}Mn_{0.03}S$ QDs which possesses the mixture of spherical, square, and hexagonal shaped structure with un-even grain size. The shape and size of the particles / grains in the Mn-doped ZnS QDs are irregular and chaotic nature. Figure 4b shows the morphology of $Zn_{0.958}Mn_{0.03}Cr_{0.02}S$ QDs. It is detected from Fig. 4b that during the incorporation of Cr in $Zn_{0.97}Mn_{0.03}S$, the morphology of the agglomerations be likely to be more spherical with considerable reduction in size. TEM micrograph of $Zn_{0.958}Mn_{0.03}Cr_{0.02}S$ QDs displays the small sized grains distributed over the microstructures due to the drop off of its surface energy by Cr addition.

TEM is employed to explore the minerals at elevated magnifications, with significant added information presented by selected-area electron diffraction (SAED) patterns. SAED patterns are particularly helpful for the examination of minute crystals and partially disordered material with few hundred \AA . SAED pattern of $Zn_{0.97}Mn_{0.03}S$ and $Zn_{0.958}Mn_{0.03}Cr_{0.02}S$ nanostructures are in Fig. 4c and d, respectively. The three rings corresponding to $(h k l)$ orientations agreed well with the XRD pattern. Among the three orientations, namely, (111), (22) and (311), the (111) orientation is very bright which verifies the prime peak value of XRD. Adjacent orientations are similar successive peaks of XRD pattern. All SAED patterns convey the cubic phase of the prepared samples, which is in better agreement with the noticed XRD pattern.

3.3. EDX - Compositional Analysis

EDX examination has been taken out to evaluate the basic element composition and the basic elements like Zn, S, Mn and Cr of the samples [63] with an appropriate stoichiometric composition. The basic and fundamental elemental mapping analysis of Mn/Cr doped ZnS by EDX spectra is presented in Fig. 5. The inset of Fig. 5 exhibits the atomic % of the elements like Zn, Mn, Cr and S in Mn/Cr doped ZnS nanostructures. The quantitative examination of atomic % of the elemental composition in of $Zn_{0.97}Mn_{0.03}S$ and $Zn_{0.95}Mn_{0.03}Cr_{0.02}S$ nanostructures using EDX investigation is presented in Table 2.

Mn / (Zn + Mn + Cr) ratio is found to be 2.94% and 3.05% for $Zn_{0.97}Mn_{0.03}S$ and $Zn_{0.95}Mn_{0.03}Cr_{0.02}S$ nanostructures, respectively. Moreover, Cr / (Zn + Mn + Cr) ratio derived in $Zn_{0.95}Mn_{0.03}Cr_{0.02}S$ is $\approx 2.04\%$. The atomic % of Zn gradually decreased and also Cr level enhanced by Cr substitution which evidently

indicates that the Cr ions are properly substituted into Zn-Mn-S lattice. The experimental results are almost equivalent to their stoichiometry with the least amount variation from the real values.

3.4. X-ray photoelectron spectroscopy (XPS)

XPS is useful to explore the doping elements and verify the valence state of Zn, Mn and Cr ions in Zn-S lattice at their equivalent binding energy. Figure 6 presents the derived XPS spectra of the Zn 2p, Mn 2p and Cr 2p core levels. The presence of Mn and Cr is confirmed by Mn 2p and Cr 2p XPS peaks.

Figure 6a shows the overall XPS spectra of Mn, Cr doped ZnS which contains the peaks corresponding to S^{2-} , Cr^{3+} , Mn^{2+} and Zn^{2+} . The higher resolution spectra of XPS spectra of Cr 2p have been revealed in the inset of Fig. 6 (a) where the peak of Cr $2p_{3/2}$ is located at 577 eV [64]. The location of Cr $2p_{3/2}$ peak is different from those of 574.2 eV corresponding to Cr metal, 579.0 eV for Cr^{6+} and 576.0 eV for Cr^{2+} , however it is close to the location of Cr $2p_{3/2}$ (576.7 eV) in Cr_2O_3 [43]. It recommends that the Cr elements are included into the Zn-S lattice as Cr^{3+} ions. The intensity of Cr $2p_{1/2}$ peak is higher than Cr $2p_{3/2}$. The main reason is the presence of XPS photoelectron corresponding to Cr $2p_{1/2}$ situated at 585.2 eV [65].

Figure 6b shows the Zn 2p spectra of Mn/Cr-doped ZnS which exhibits two peaks, first peak around 1022 eV corresponding to $2p_{3/2}$ and the another peak around 1046 eV corresponding to $2p_{1/2}$. The peak locations corresponding to $2p_{3/2}$ and $2p_{1/2}$ state of Zn confirms the existence of Zn^{2+} , which accurately equivalent to the binding energy of Zn-S bonding [66]. The peak corresponding to S 2p state with binding energy around 162 eV as in Fig. 6 confirms the occurrence of Zn^{2+} in Zn-S lattice [67]. The existence of Mn is confirmed from the Mn 2p spectra within the binding energy range of 630–660 eV as displayed in Fig. 6(c). It is noticed from Fig. 6c that the intensity of Mn 2p state is weak. The observed peaks in the region of 642 eV and 654.2 eV related to the Mn 2p spectra verify the existence of Mn in the Zn-Cr-S lattice and these Mn^{2+} ions could play as substitutes for the Zn atoms or as interstitial one [48].

3.5. Optical studies

Generally, the optical characters of the QDs were studied by the optical absorption performance of the materials. The absorption of $Zn_{0.97}Mn_{0.03}S$ and $Zn_{0.95}Mn_{0.03}Cr_{0.02}S$ nanostructures between the wavelength around 310–550 nm is illustrated as shown in Fig. 7a. Mn-doped ZnS ($Zn_{0.97}Mn_{0.03}S$) nanostructures exhibit a higher absorption along UV wavelength region i.e., below 360 nm and exhibit a sudden fall off at upper wavelength region. The inclusion of Cr^{3+} into $Zn_{0.97}Mn_{0.03}S$ diminishes the absorption intensity. The present decrease in absorption intensity may possibly be ascribed to the introduction of defects and lattice imperfections in the Zn-Mn-S lattice structure from the different ionic sizes of Zn^{2+} , Cr^{3+} , and Mn^{2+} . Moreover, the reduction in intensity may also originate from the scattered light along the grain boundaries and the cluster of Cr^{3+} in the lattice [68]. In addition to the shrinkage of absorption intensity, the inclusion of Cr^{3+} ions induce the absorption edge moving along the higher frequency region i.e., the higher energy region (blue shift). The current blue shift of absorption edge and

the shrinkage of absorption intensity are also supported by the size decrement which is presented in Table 1. Moreover, the blue shift of absorption edge indicates the increase of energy gap of the material.

The energy gap of Mn-doped and Mn-Cr co-doped ZnS nanostructures have been derived with the help of the plot among $(\alpha h\nu)^2$ versus $h\nu$ [69] as revealed in Fig. 7b. The energy gap of pure ZnS from literature is found to be 3.67 eV at ambient temperature [70]. The energy gap of Mn = 3% doped ZnS ($\text{Zn}_{0.97}\text{Mn}_{0.03}\text{S}$) obtained from Fig. 7b is 3.5 eV which is ~ 0.17 eV ($\Delta E_g \sim 0.17$ eV) smaller than ZnS. The 3d electrons existing in Mn interact with the electrons in Zn which creates the dislocation / imperfections in the structural bonding of ZnS [31]. The induced interaction among the 's' and 'p' electrons existing in ZnS and '3d' electrons in Mn^{2+} ions is accountable for the present decrease in band gap [71]. The incorporation of Mn into Zn-S also creates some new energy levels nearer to the valence level of ZnS which is also the additional probable reason for the present decrease in band gap [72].

The rapid increase of band gap from 3.50 eV ($\text{Zn}_{0.97}\text{Mn}_{0.03}\text{S}$) to 3.63 eV ($\text{Zn}_{0.95}\text{Mn}_{0.03}\text{Cr}_{0.02}\text{S}$, $\Delta E_g \sim 0.13$ eV) is achieved by adding Cr where, Cr^{3+} ions with smaller ionic radius can be restore Zn^{2+} ions in the substitutional sites. The substitution of Cr in Zn-Mn-S lattice releases additional free carriers which alter the Fermi level and shift nearer to the conduction level and widen the energy gap. The enhanced energy gap (blue shift) during Cr doping is explained by the Burstein-Moss shift [73, 74]. The decrease of size is also play a main role in the elevation of band gap [75].

3.6. Fourier transform infrared (FTIR) studies

The FTIR spectra of $\text{Zn}_{0.97}\text{Mn}_{0.03}\text{S}$ and $\text{Zn}_{0.95}\text{Mn}_{0.03}\text{Cr}_{0.02}\text{S}$ nanostructures are presented in Fig. 8 from 400 cm^{-1} to 4000 cm^{-1} and their wave number assignments are listed in Table 3. The wide and the broad absorption bands in the synthesized samples within the wave number range of $3350\text{--}3450\text{ cm}^{-1}$ are associated to O-H stretching vibration of water [4]. The strong absorption bands $\sim 1574\text{--}1598\text{ cm}^{-1}$ are accountable for O-H bending vibration [76]. The bands around 1122 cm^{-1} and $1023\text{--}1026\text{ cm}^{-1}$ are correlated to the substitution of Cr / Mn in Zn location and the micro-structural Mn/Cr in Zn-S matrix [4]. The weak band located around 939 cm^{-1} represents the imperfection / defects stimulated by Cr-substitution in Zn-Mn-S matrix which is not present in $\text{Zn}_{0.97}\text{Mn}_{0.03}\text{S}$ [54]. The characteristic bands about $674\text{--}676\text{ cm}^{-1}$ and $492\text{--}519\text{ cm}^{-1}$ are corresponding to Zn-S stretching vibrations [77]. The bands corresponding to Zn-S show the better agreement with the earlier studies [78]. A close resemblance of the two FTIR spectra (without and with Cr-doped $\text{Zn}_{0.97}\text{Mn}_{0.03}\text{S}$) specifies that Cr^{3+} ions have substituted into ZnS.

3.7. Photoluminescence (PL) spectra

PL is the main optical characteristics for different PL nano-materials, like nano-sized particles and QDs [79–82]. Figure 9a illustrates the PL spectra of ZnS from 350 nm to 650 nm at room temperature. ZnS shows a wide PL peak from 370 to 550 nm as explained by Faita et al. [83]. The addition of Mn and Cr strongly modified the intensity and peak position. Figure 9b and c reveals the PL emissions of without

and with Cr-doped $\text{Zn}_{0.97}\text{Mn}_{0.03}\text{S}$ nanostructures from 345 to 700 nm. Figure 9b contains a strong near violet (NV) emission at 388 nm. Even though, no major change in peak position of UV band is noticed, peak intensity is decreased by Cr = 2% doping. Generally, the luminescence in the visible region arises from impurity or native defect associated transitions [84]. The present NV band is originated from the nano-sized particles and the stimulated defects like Zn / S interstitials. Here, various peaks are combined into a single and broad band at 388 nm [85]. The similar shrinkage of PL intensity was described by Nasser et al. [31] in Mn-ZnS and they explained that the reducing band-band recombination rate is accountable for the reduced PL intensity.

Figure 9c illustrates the PL spectra of $\text{Zn}_{0.97}\text{Mn}_{0.03}\text{S}$ and $\text{Zn}_{0.95}\text{Mn}_{0.03}\text{Cr}_{0.02}\text{S}$ nanostructures between 500 and 700 nm. Both samples exhibit a band corresponding to yellowish-orange wavelength at 594 nm. Figure 9c reflected that PL intensity is shifted to higher side by Cr addition in $\text{Zn}_{0.97}\text{Mn}_{0.03}\text{S}$. A band at 594 nm is due to the exchange communication among the s-p electron states of Cr^{3+} , Mn^{2+} and Zn^{2+} ions in Zn-S [86–88]. Figure 10 represents the energy level diagram of Cr-doped $\text{Zn}_{0.97}\text{Mn}_{0.03}\text{S}$ to describe the different emissions such as NV and yellowish orange. The dominant visible emission band emerged ~ 594 nm is initiated from the electronic switch over from ${}^4\text{T}_1$ level to ${}^6\text{A}_1$ level in the 3d configuration of Mn^{2+} / Cr^{3+} ions [89, 90]. The emissions at 580–600 nm was also described by Kole et al. [91] and Karar et al. [92]. It is implied from Fig. 10 that the charge carriers may relax to the defect positions, from which they recombine via the d-orbital of Cr^{3+} or be transferred to Mn^{2+} states that lead to the characteristic Cr^{3+} and Mn^{2+} emissions [93]. The obtained elevated yellowish-orange wavelength emission in Mn/Cr substituted ZnS highlights their applications optical devices like organic LEDs and solar cells.

4. Conclusions

Mn added ZnS ($\text{Zn}_{0.97}\text{Mn}_{0.03}\text{S}$) and Mn-Cr co-doped ZnS ($\text{Zn}_{0.95}\text{Mn}_{0.03}\text{Cr}_{0.02}\text{S}$) nanostructures were synthesized using co-precipitation route. XRD patterns confirmed the cubic structure in all the samples and preferred orientation through (111) direction. The shrinkage in crystallite size from 36 Å ($\text{Zn}_{0.97}\text{Mn}_{0.03}\text{S}$) to 26 Å ($\text{Zn}_{0.95}\text{Mn}_{0.03}\text{Cr}_{0.02}\text{S}$) and effect of Cr and Mn substitution on morphology, optical and PL properties in ZnS have been investigated. The substitution of Cr in Zn-Mn-S lattice not only diminished the size and also produced more defect associated luminescent centres. The survival of Zn^{2+} , Mn^{2+} and Cr^{3+} ions in Zn-Mn-Cr-S lattice is verified by XPS spectra. The energy gap enhancement by Cr doping was elucidated by Burstein–Moss effect and reduced crystallite size. The tuning of energy gap and size by Mn/Cr substitution encourages these materials for electronic device applications. FTIR spectra verified the existence of Mn/Cr in Zn-S lattice by their fundamental characteristic bondings. The Mn /Cr doping provides an efficient control over modification of various emission colours which suggests their applications in organic light emitting diode materials.

References

1. G. Alvarez-Coronado, L.A. González, J.C. Rendón-Ángeles, M.A. Meléndez-Lirab, R. Ramírez-Bon, *Mat. Sci. Semicon. Proc.* 81 (2018) 68–74.
2. A. Ruffner, M.D. Hilmel, V. Mizrahi, G.I. Stegeman, U. Gibson, *J. Appl. Opt.* 28 (1989) 5209–5214.
3. Göde, C. Gümüş, M. Zor, *J. Cryst. Growth* 299 (2007) 136–141.
4. Ummartyotin, N. Bunnak, J. Juntaro, M. Sain, H. Manuspiya, *Solid State Sci.* 14 (2012) 299–304.
5. Yang, J. Sun, X. Li, W. Zhou, Z. Wang, P. He, G. Ding, X. Xie, Z. Kang, M. Jiang, *J. Mater. Chem. A* 2 (2014) 8660-8667.
6. Yang, J. Sun, P. He, X. Deng, Z. Wang, C. Hu, G. Ding, X. Xie, *Chem. Mater.* 27 (2015) 2004-2011.
7. Wang, Q. Guo, D. Chen, Z. Liu, X. Zheng, A. Xu, S. Yang, G. Ding, *ACS appl. Mater. Interfaces* 10 (2018) 5750-5759.
8. Huang, S. Yang, Q. Li, Y. Yang, G. Wang, X. You, B. Mao, H. Wang, Y. Ma, P. He, Z. Liu, G. Ding, X. Xie, *Langmuir* 34 (2018) 250-258.
9. Yang, Y. Yang, P. He, G. Wang, G. Ding, X. Xie, *Langmuir* 33 (2017) 913-919.
10. Zhu, S. Yang, G. Wang, R. Mo, P. He, J. Sun, Z. Di, Z. Kang, N. Yuan, J. Ding, G. Ding, X. Xie, *J. Mater. Chem. B* 3 (2015) 6871-6876.
11. Yang, W. Li, C. Ye, G. Wang, H. Tian, C. Zhu, P. He, G. Ding, X. Xie, Y. Liu, Y. Lifshitz, S. Lee, Z. Kang, M. Jiang, *Adv. Mater.* 29 (2017) 1605625.
12. Xu, G. Wang, Y. Li, H. Dong, S. Yang, P. He, G. Ding, *Small* 16 (2020) 2004621
13. Li, S. Yang, Z. Liu, G. Wang, P. He, W. Wei, M. Yang, Y. Deng, P. Gu, X. Xie, Z. Kang, G. Ding, H. Zhou, X. Fan, *Adv. Mater.* 33 (2021) 2005096.
14. Wageh, L. Shu-Man, F. Tian You, X. Rong, *J. Lumin.* 102-103 (2003) 768-773.
15. Hedayat, J. *Nanostruct.* 5 (2015) 395-401.
16. A. Rosli, Z.A. Zubir, N.M.A. Aziz, *Adv. Mater. Res.* 364 (2012) 434-438.
17. Seodi, A. Shabaka, W.H. Eisa, B. Anies, N.M. Farage, *Physica B* 405 (2010) 919-924.
18. Borah, K. Sarma, *Acta Phys. Pol. A* 114 (2008) 713-719.
19. Haddad, A. Chelouche, D. Talantikite, H. Merzouk, F. Boudjouan, D. Djouadi, *Thin Solid Films* 589 (2015) 451–456.
20. S. Karan, S. Sarkar, D.D. Sarma, P. Kundu, N. Ravishankar, N. Pradhan, *J. Am. Chem. Soc.* 133 (2011) 1666–1669.
21. K. Salem, T.M. Hammad, S. Kuhn, M.A. Draaz, N.K. Hejazy, R. Hempelmann, *J. Mater. Sci. Mater. Electron.* 25 (2014) 2177–2182.
22. Diaz-Reyes, R. Castillo-Ojeda, R. Sánchez-Espíndola, M. Galván-Arellano, O. Zaca-Morán, *Curr. Appl. Phys.* 15 (2015) 103–109.
23. Wang, H. Huang, B. Liang, Z. Liu, D. Chen, G. Shen, *Crit. Rev. Solid State Mater. Sci.* 38 (2013) 57–90.
24. Daranf, M. Aida, A. Hafdallah, H. Lekiket, *Thin Solid Films* 518 (2009) 1082–1084.

25. C. Erwin, L. Zu, M.I. Haftel, A.L. Efros, T.A. Kennedy, D.J. Norris, *Nature* 436 (7047) (2005) 91–94.
26. Bera, L. Qian, T.K. Tseng, P.H. Holloway, *Materials* 3 (4) (2010) 2260–2345.
27. Huang, Y. Cai, H. Liu, *Particuology* 9 (2011) 533–536.
28. Falcony, M. Garcia, A. Ortiz, J. Alonso, *J. Appl. Phys.* 72 (1992) 1525–1527.
29. Cao, D. Han, B. Wang, L. Fan, H. Fu, M. Wei, B. Feng, X. Liu, J. Yang, *J. Solid State Chem.* 200 (2013) 317–322.
30. Viswanath, H.B. Naik, G.Y. Kumar, P.P. Kumar, G.A. Kumar, R. Praveen, *J. Lumin.* 153 (2014) 446–452.
31. Ebrahimi, B. Yarmand, N. Naderi, *Thin Solid Films* 676 (2019) 31–41.
32. Ma, J. Song, Z. Yu, *Thin Solid Films* 519 (2011) 5043–5045.
33. Geszke-Moritz, H. Piotrowska, M. Murias, L. Balan, M. Moritz, J. Lulek, R. Schneider, *J. Mater. Chem. B* 1 (2013) 698–706.
34. Labiadh, B. Sellami, A. Khazri, W. Saidani, S. Khemais, *Opt. Mater.* 64 (2017) 179–186.
35. Huang, L. Wang, K. Tang, M. Lin, Y. Yu, X. Lu, Y. Xia, *Surf. Coat. Technol.* 228 (2013) S397–S400.
36. B. Cruz, Q. Shen, T. Toyoda, *Thin Solid Films* 499 (2006) 104–109.
37. Bhargava, D. Gallagher, X. Hong, A. Nurmikko, *Phys. Rev. Lett.* 72 (1994) 416.
38. Kripal, A.K. Gupta, S.K. Mishra, R.K. Srivastava, A.C. Pandey, S. Prakash, *Spectrochim. Acta Part A.* 76 (2010) 523–530.
39. Jrad, W. Naffouti, T.B. Nasr, S. Ammar, N. Turki-Kamoun, *J. Mater. Sci. Mater. Electron.* 28 (2017) 1463–1471.
40. Goudarzi, G.M. Aval, S.S. Park, M.-C. Choi, R. Sahraei, M.H. Ullah, A. Avane, C.-S. Ha, *Chem. Mater.* 21 (2009) 2375–2385.
41. Nasser, H. Elhouichet, M. Férid, *Appl. Surf. Sci.* 351 (2015) 1122–1130.
42. C. Sebastian, M. Chawda, L. Jonny, D. Bodas, *Mater. Lett.* 64 (2010) 2269–2272.
43. Q. Wang, J. Iqbal, X.D. Shan, G.W. Huang, H.G. Fu, R.H. Yu, D.P. Yu, *Mater. Chem. Phys.* 113 (2009) 103–106.
44. Sato, H. Yoshida, *J. Appl. Phys.* 39 (2000) L555–L558.
45. Poornaprakash, K. Naveen Kumar, U. Chalapathi, M. Reddeppa, P.T. Poojitha, Si-Hyun Park, *J. Mater. Sc. Mater. Electron.* 27 (2016) 6474–6479.
46. Aqeel, M. Ikram, A. Asghar, A. Haider, A. Ul-Hamid, M. Naz, M. Imran, S. Ali, *Appl. Nanoscience* 10 (2020) 2045–2055.
47. A. Reddy, A. Divya, G. Murali, R.P. Vijayalakshmi, B.K. Reddy, *Physica B* 406 (2011) 1944–1949.
48. Yang, M. Lu, G. Zhou, D. Yuan, D. Xu, *Inorg. Chem. Commun.* 4 (2001) 734–737.
49. Z. Liu, P.X. Yan, G.H. Yue, J.B. Chang, D.M. Qu, R.F. Zhuo, *J. Phys. D: Appl. Phys.* 39 (2006) 2352–2356.
50. Yang, M. Lu, D. Xu, D. Yuan, C. Song, S. Liu, X. Cheng, *Opt. Mater.* 24 (2003) 497–502.

51. W. Lee, K. Cho, H. Kim, J.-H. Kim, B. Park, T. Noh, S.H. Kim, S. Kim, *Jpn. J. Appl. Phys.* 44 (2005) 7694–7697.
52. Ma, W. *Chen Nanotechnology* 21 (2010) 385604–385611.
53. Wang, F. Huang, Y. Xia, A. Wang, *J. Lumin.* 128 (2008) 610–614.
54. Sakthivel, S. Muthukumaran, *J. Phys. Chem. Solids* 120 (2018) 183–189.
55. Kaur, S. Kumar, A. Singh, C.L. Chen, C.L. Dong, T.S. Chan, K.P. Lee, C. Srivastava, S.M. Rao, M.K. Wu, *Superlattices Microstruct.* 83 (2015) 785–795.
56. B. Duan, X.R. Zhao, J.M. Liu, T. Wang, G.H. Rao, *Appl. Phys. A* 99 (2010) 679–683.
57. Sakthivel, S. Muthukumaran, *Opt. Laser Technol.* 103 (2018) 109–117.
58. Anbuselvan, S. Muthukumaran, *Opt. Mater.* 42 (2015) 124–131.
59. P. Ravaro, D.I. Santos, L.V.A. Scalvi, *J. Phys. Chem. Solids* 70 (2009) 1312–1316.
60. Bhargava, P.K. Sharma, S. Kumar, A.C. Pandey, N. Kumar, *J. Solid State Chem.* 183 (2010) 1400–1408.
61. Ozgur, Y. Alivov, C. Liu, A. Teke, M.A. Reshchikov, S. Dogan, V.A. Cho, H. Morkoc, *J. Appl. Phys.* 98 (2005) 041301.
62. Yilmaz, M. Parlak, S. Ozcan, M. Altunbas, E. McGlynn, E. Bacaksiz, *Appl. Surf. Sci.* 257 (2011) 9293–9298.
63. Johny Basha, V. Khidhirbrahmendra, J. Madhavi, U.S. Udayachandran Thampy, Ch. Venkata Reddy, R.V.S.S.N. Ravikumar, *J. Sci. Adv. Mater. Dev.* 4 (2019) 260–266.
64. Liu, Y. Yang, J. Yang, Q. Guan, H. Liu, L. Yang, Y. Zhang, Y. Wang, M. Wei, X. Liu, L. Fei, X. Cheng, *J. Solid State Chem.* 184 (2011) 1273–1278.
65. Prathap, N. Revathi, Y.P. Venkata Subbaiah, K.T. Ramakrishna Reddy, *J. Phys.: Condens. Matter.* 20 (2008) 035205.
66. W. Shin, S.R. Kang, J.H. Yun, A.V. Moholkar, J.H. Moon, J.Y. Lee, J.H. Kim, *Sol. Energy Mater. Sol. Cells* 95 (2011) 856–863.
67. Asenjo, A.M. Chaparro, M.T. Gutierrez, J. Herrero, J. Klaer, *Sol. Energy Mater. Sol. Cells* 92 (2008) 302–306.
68. A. Reddy, G. Murali, B. Poornaprakash, R.P. Vijayalakshmi, B.K. Reddy, *Appl. Surf. Sci.* 258 (2012) 5206–5211.
69. Theyvaraju, S. Muthukumaran, *Physica E* 74 (2015) 93–100.
70. Firdous, M. Aslam Baba, D. Singh, A.H. Bhat, *Appl. Nanosci.* 5 (2015) 201–206.
71. K. Ghosh, S.F. Ahmed, S. Jana, K.K. Chattopadhyay, *Opt. Mater.* 29 (2007) 1584–1590.
72. Mote, Y. Purushotham, B. Dole, *Cerâmica* 59 (2013) 614–619.
73. Yang, X. Zhao, X. Shan, H. Fan, L. Yang, Y. Zhang, *J. Alloys Compd.* 556 (2013) 1–5.
74. Kumar, S. Chatterjee, K.K. Chattopadhyay, A.K. Ghosh, *J. Phys. Chem. C* 116 (2012) 16700–16708.
75. T. Tan, B.J. Chen, X.W. Sun, W.J. Fan, H.S. Kwok, X.H. Zhang, S.J. Chua, *J. Appl. Phys.* 98 (2005) 013505.

76. Nakamoto, Infrared and Raman spectra of inorganic and coordination compounds, Parts-A and B. Wiley, New York, 1997.
77. S. Rema Devi, R. Raveendran, A.V. Vaidyan, Pramana—J. Phys. 68 (2007) 679–687.
78. Tong, Z. Jiang, C. Wang, Z.Y. Xin, S. Hong, Liu, Mater. Lett. 62 (2008) 3385-3387.
79. R. Reddy, K.P. Lee, J.Y. Kim, Y. Lee, J. Nanosci. Nanotechnol. 8 (2008) 5632– 5639.
80. R. Reddy, H.M. Jeong, Youngil Lee, A.V. Raghu, J. Polym. Sci. Part A Polym. Chem. 48 (2010) 1477–1484.
81. Hassan, E. Haque, K.R. Reddy, A.I. Minett, J. Chen, V.G. Gomes, Nanoscale. 6 (2014) 11988–11994.
82. P. Alivisatos, Semiconductor clusters, nanocrystals, and quantum dots, Science 27 (1996) 1933–1937.
83. L. Faita, K. Ersching, C.M. Poffo, L.C. Benetti, D.M. Trichês, S.M. Souza, A.D.C. Viegas, J.C. de Lima, J. Alloys Compd. 590 (2014) 176-183.
84. Pan, D. Yang, Y. Zhao, Z. Ma, G. Dong, J. Qiu, J. Alloys Compd. 579 (2013) 300–304.
85. Bhattacharjee, Ch.-H. Lu, Thin Solid Films 514 (2006) 132–137.
86. Zeng, J. Zhang, F. Huang, J. Appl. Phys. 111 (2012) 123525.
87. Kaur, M. Sharma, O.P. Pandey, Opt. Mater. 47 (2015) 7–17.
88. Xia, I.W. Lenggoro, K. Okuyama, Chem. Mater. 14 (2002) 4969–4974.
89. Dong, L. Cao, G. Su, W. Liu, J. Colloid Interface Sci. 367 (2012) 178–182.
90. Datta, S. Biswas, S. Kar, Nanosci. Nanotechnol. 10 (2007) 3670–3676.
91. Kole, C. Tiwary, P. Kumbhakar, J. Appl. Phys. 113 (2013) 114308.
92. Karar, F. Singh, B. Mehta, J. Appl. Phys. 95 (2004) 656–660.
93. Wang, M. Yang, Y. Ren, J Fan, Anal. Chim. Acta 1040 (2018) 136-142.

Tables

Table 1 The peak intensity, peak position (2 θ), FWHM, β value, d-value, lattice parameter 'a', crystallite size (D) and micro strain (ϵ) along (111) plane of Zn_{0.97}Mn_{0.03}S and Zn_{0.95}Mn_{0.03}Cr_{0.02}S QDs

Samples	Peak intensity (counts)	Peak position (2 θ (°))	FWHM (β) (°)	d ₍₁₁₁₎ (Å) *	Lattice parameter, 'a' (Å) #	Crystallite size(D) (Å)	Micro strain (ϵ) x 10 ⁻³
Zn _{0.97} Mn _{0.03} S	1702	29.1	2.3	3.066	5.311	36	9.71
Zn _{0.95} Mn _{0.03} Cr _{0.02} S	1518	28.6	3.1	3.119	5.404	26	13.11

* JCPDS card No. 80-0020

a = 5.406 Å - JCPDS card No. 05-0566

Table 2 The quantitative analysis of atomic percentage of the compositional elements in of $Zn_{0.97}Mn_{0.03}S$ and $Zn_{0.95}Mn_{0.03}Cr_{0.02}S$ nanostructures using EDX analysis

Samples	Atomic percentage of the elements (%)				Mn/(Mn+Zn+Cu) ratio (%)	Cu/(Mn+Zn+Cu) ratio (%)
	Zn	S	Mn	Cu		
$Zn_{0.97}Mn_{0.03}S$	54.72	43.67	1.61	-	2.94	-
$Zn_{0.95}Mn_{0.03}Cu_{0.02}S$	53.90	43.21	1.73	1.16	3.05	2.04

Table 3 IR peaks and their assignments of $Zn_{0.97}Mn_{0.03}S$ and $Zn_{0.95}Mn_{0.03}Cr_{0.02}S$ nanostructures

Assignments	Wave number (cm ⁻¹)	
	$Zn_{0.97}Mn_{0.03}S$	$Zn_{0.95}Mn_{0.03}Cr_{0.02}S$
O-H stretching vibration of H ₂ O	3386	3438
H-O-H bending vibration of H ₂ O	1574	1598
Partial substitution of Mn/Cr in Zn-S and micro-structural changes	1023	1026, 1122
Defects induced by Cr substitution in Zn-Mn-S lattice	Nil	939
Stretching mode of Zn-S lattice	492, 674	519, 676

Figures

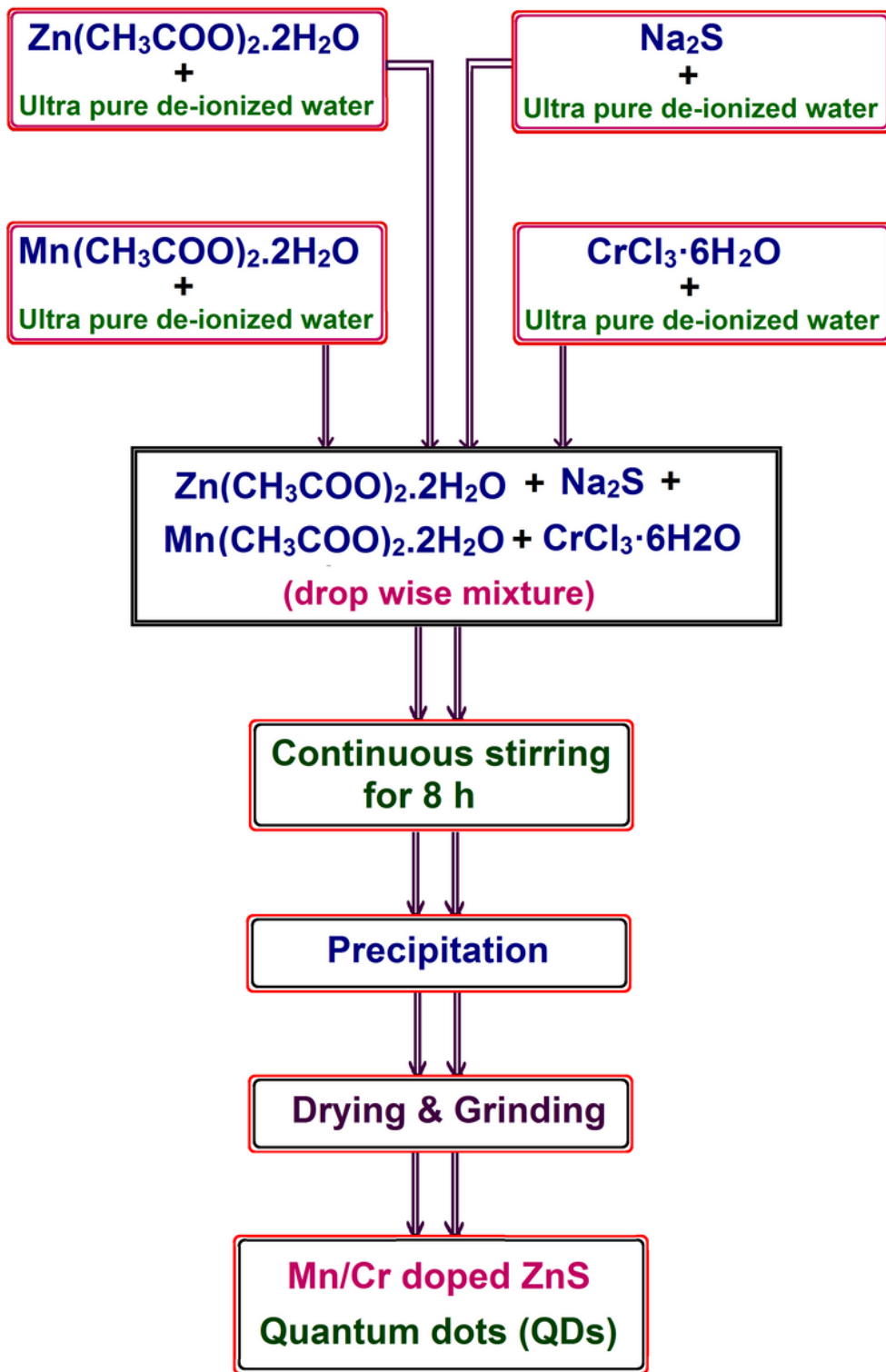


Figure 1

Flow chart for the preparation of Mn/Cr doped ZnS nanostructures using co-precipitation route

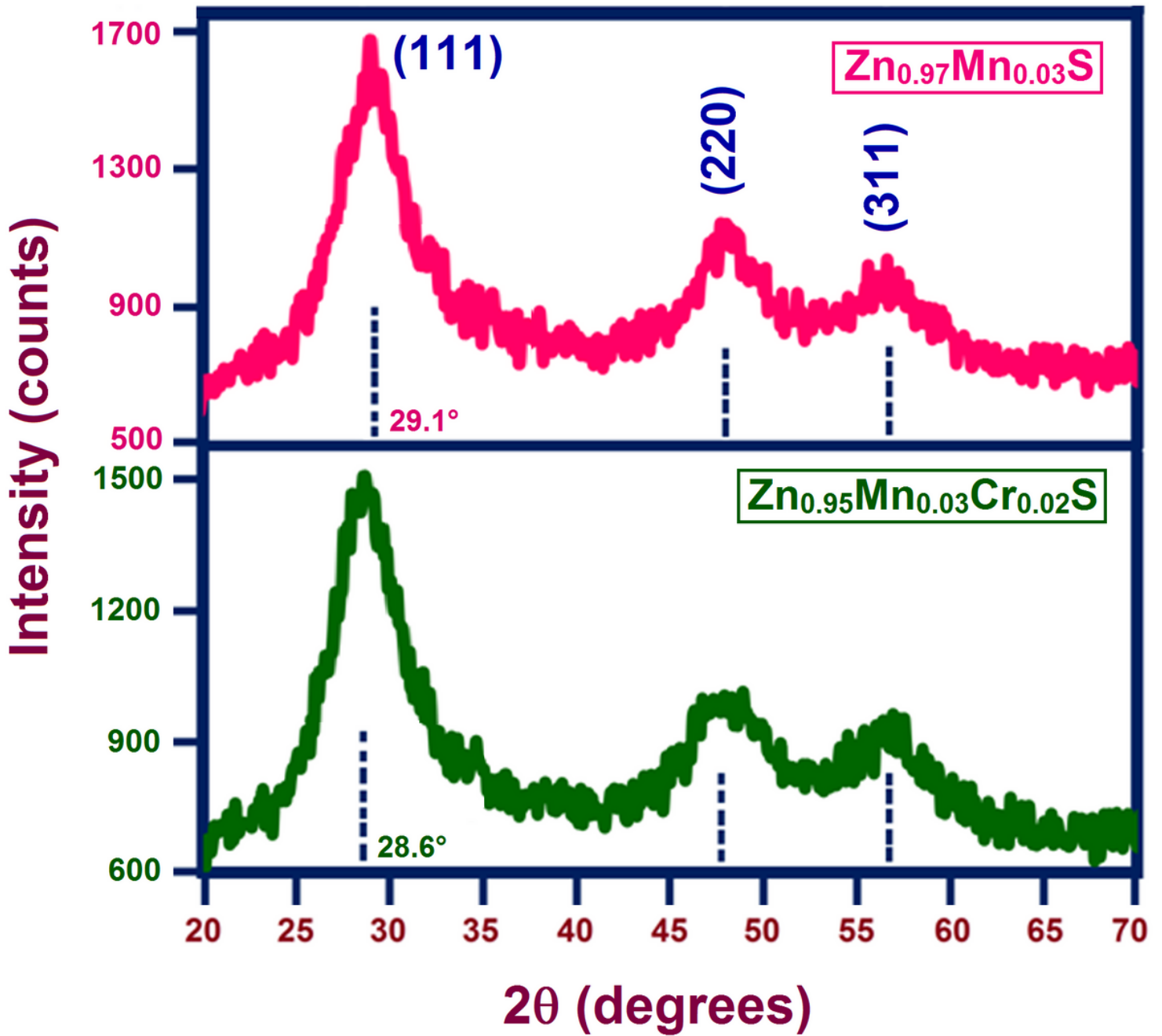


Figure 2

The XRD pattern $\text{Zn}_{0.97}\text{Mn}_{0.03}\text{S}$ and $\text{Zn}_{0.95}\text{Mn}_{0.03}\text{Cu}_{0.02}\text{S}$ nanostructures from 20° to 70°

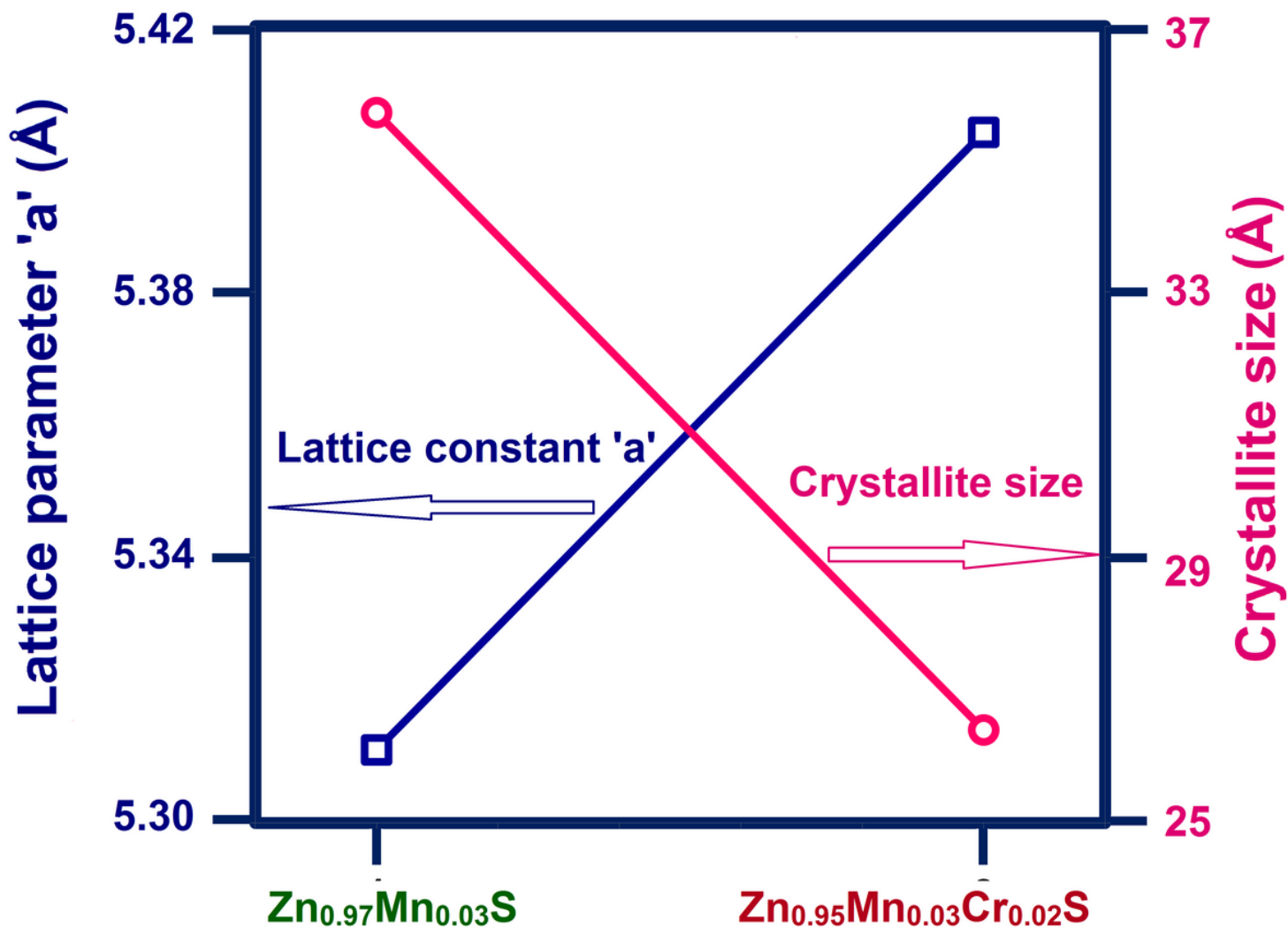


Figure 3

The variation of lattice constant 'a' and crystallite size of $Zn_{0.97}Mn_{0.03}S$ and $Zn_{0.95}Mn_{0.03}Cu_{0.02}S$ nanostructures

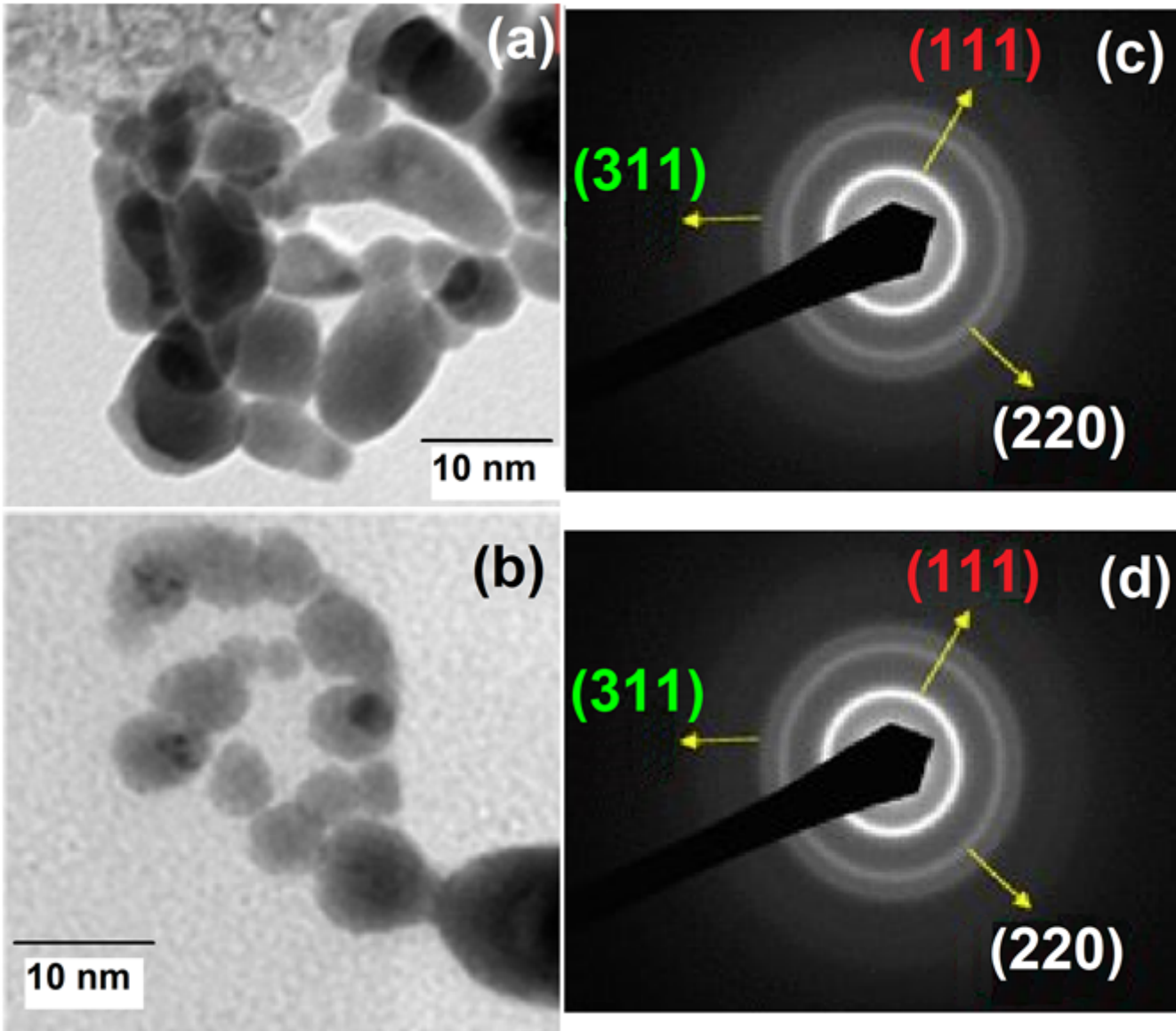


Figure 4

TEM microstructures of (a) Zn_{0.97}Mn_{0.03}S and (b) Zn_{0.95}Mn_{0.03}Cu_{0.02}S nanostructures. SAED patterns of (c) Zn_{0.97}Mn_{0.03}S and (d) Zn_{0.95}Mn_{0.03}Cu_{0.02}S nanostructures

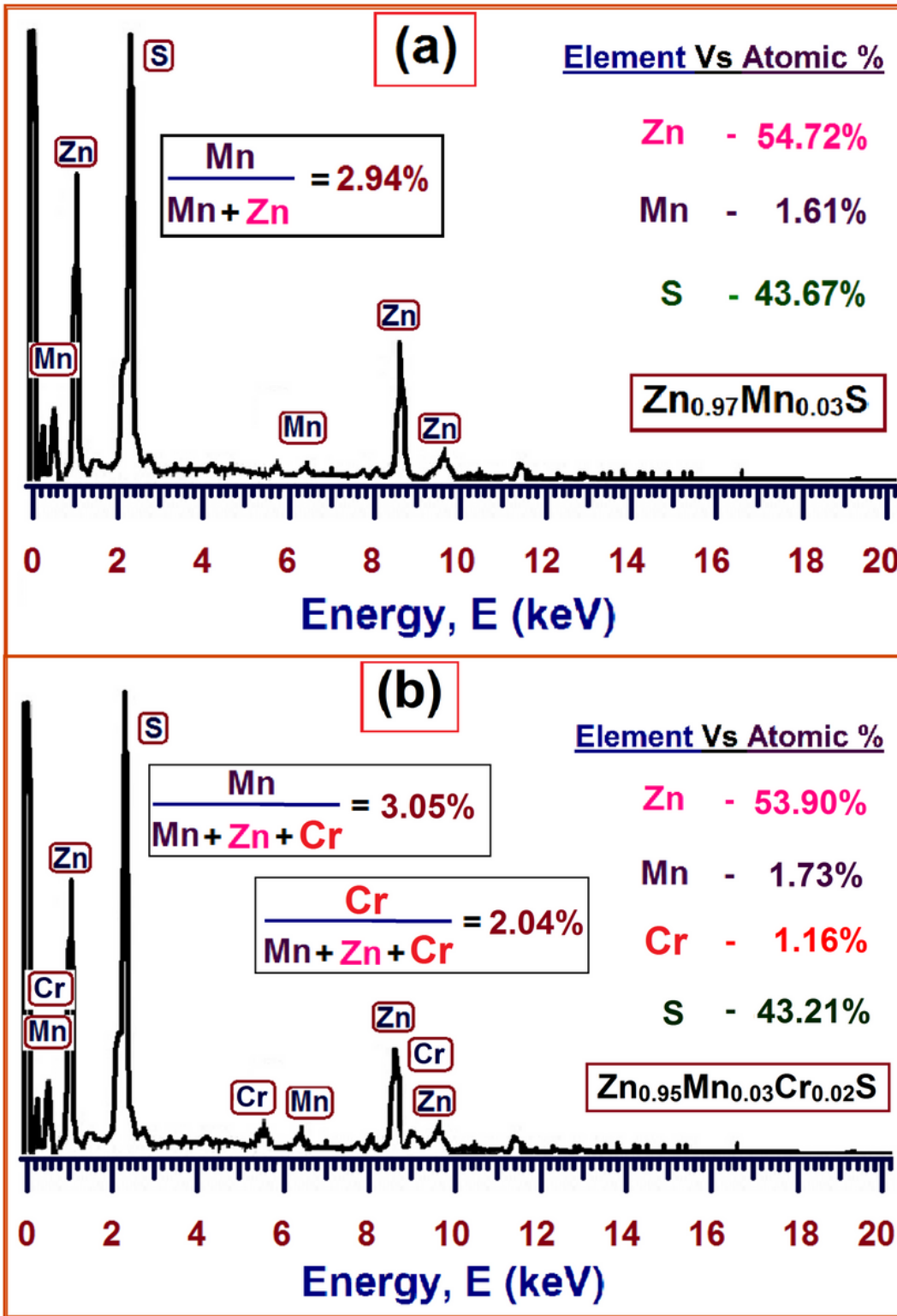


Figure 5

EDX spectra of (a) $\text{Zn}_{0.97}\text{Mn}_{0.03}\text{S}$ and (b) $\text{Zn}_{0.95}\text{Mn}_{0.03}\text{Cu}_{0.02}\text{S}$ nanostructures. The inset shows the atomic percentage of the constituent elements present in the sample

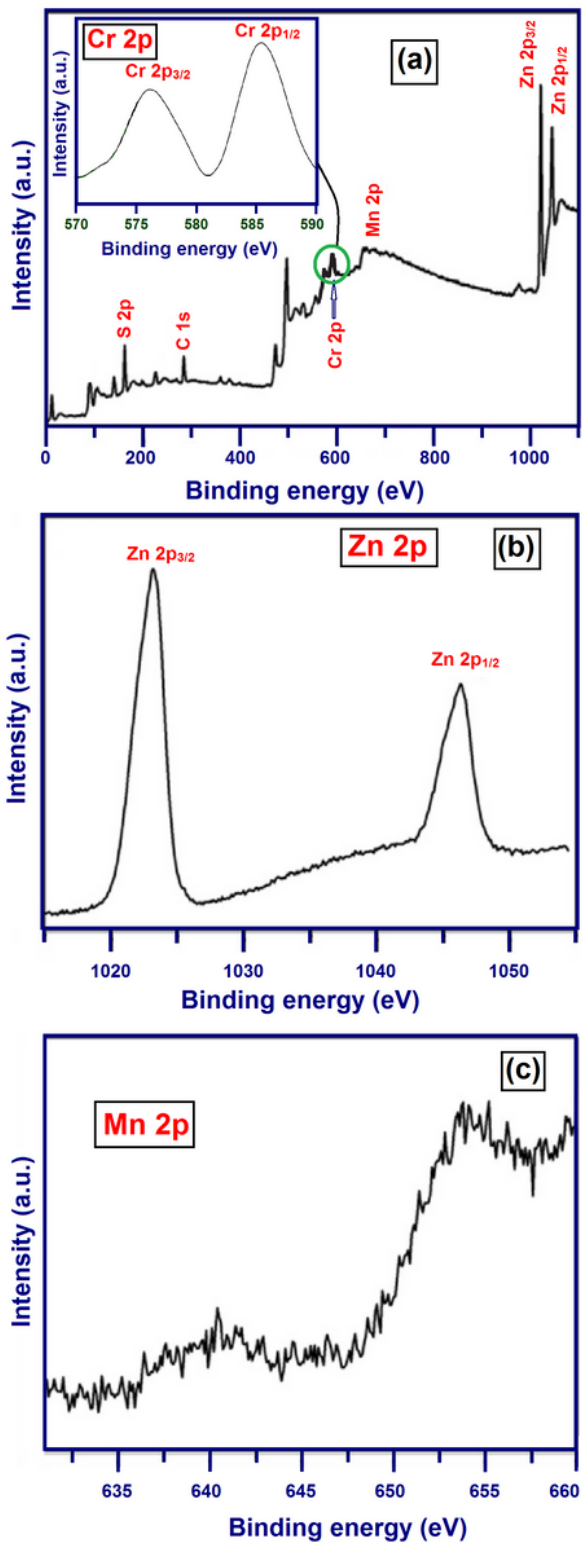


Figure 6

XPS spectra of Mn, Cr doped ZnS QDs corresponding to a) overall spectra from 0 to 1100 eV, (b) Zn 2p spectra, and c) Mn 2p spectra

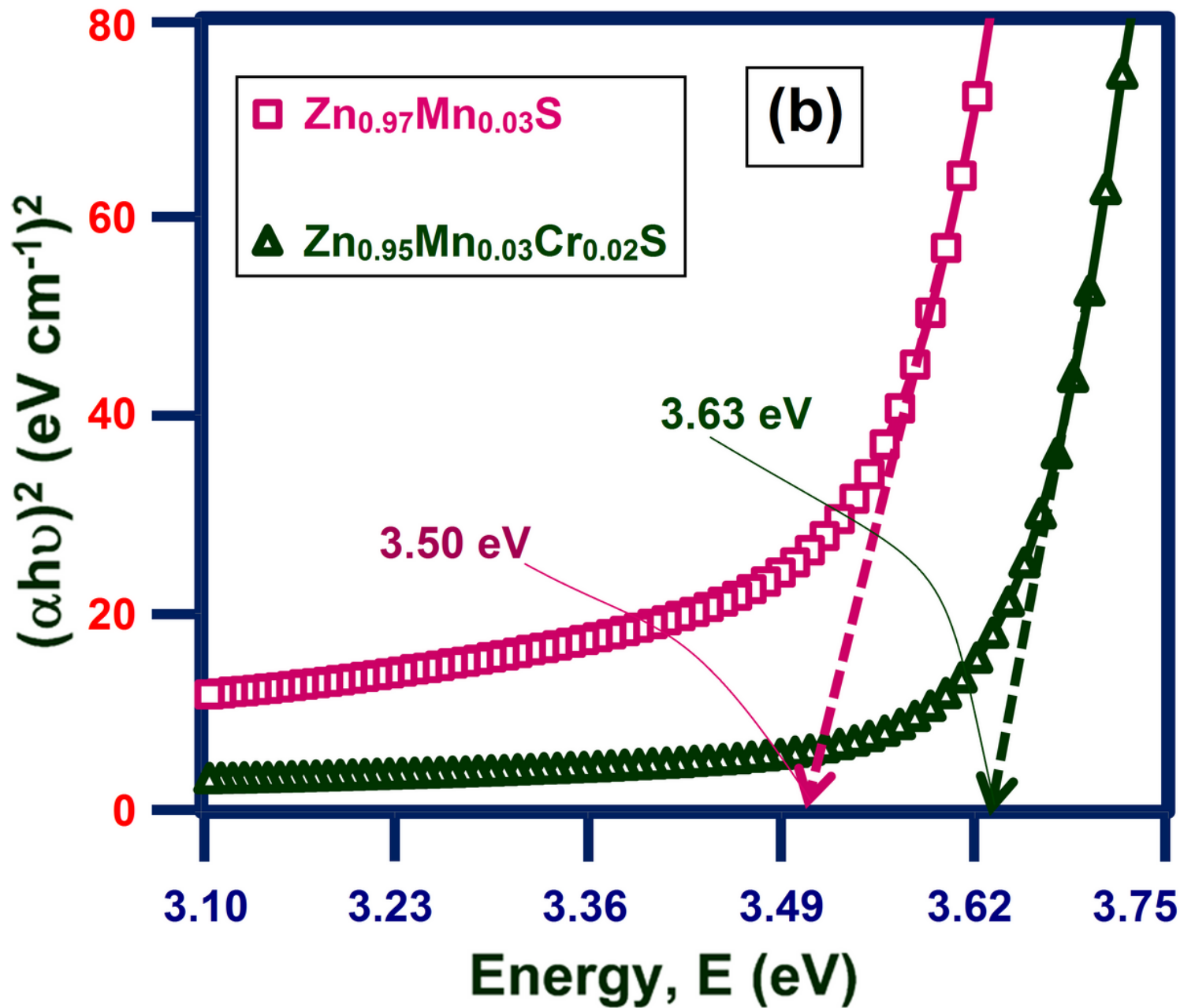


Figure 7

(a) UV-visible absorption spectra of $\text{Zn}_{0.97}\text{Mn}_{0.03}\text{S}$ and $\text{Zn}_{0.95}\text{Mn}_{0.03}\text{Cr}_{0.02}\text{S}$ from 310 to 550 nm and
 (b) $(\alpha h\nu)^2$ Vs $h\nu$ curves for band gap determination

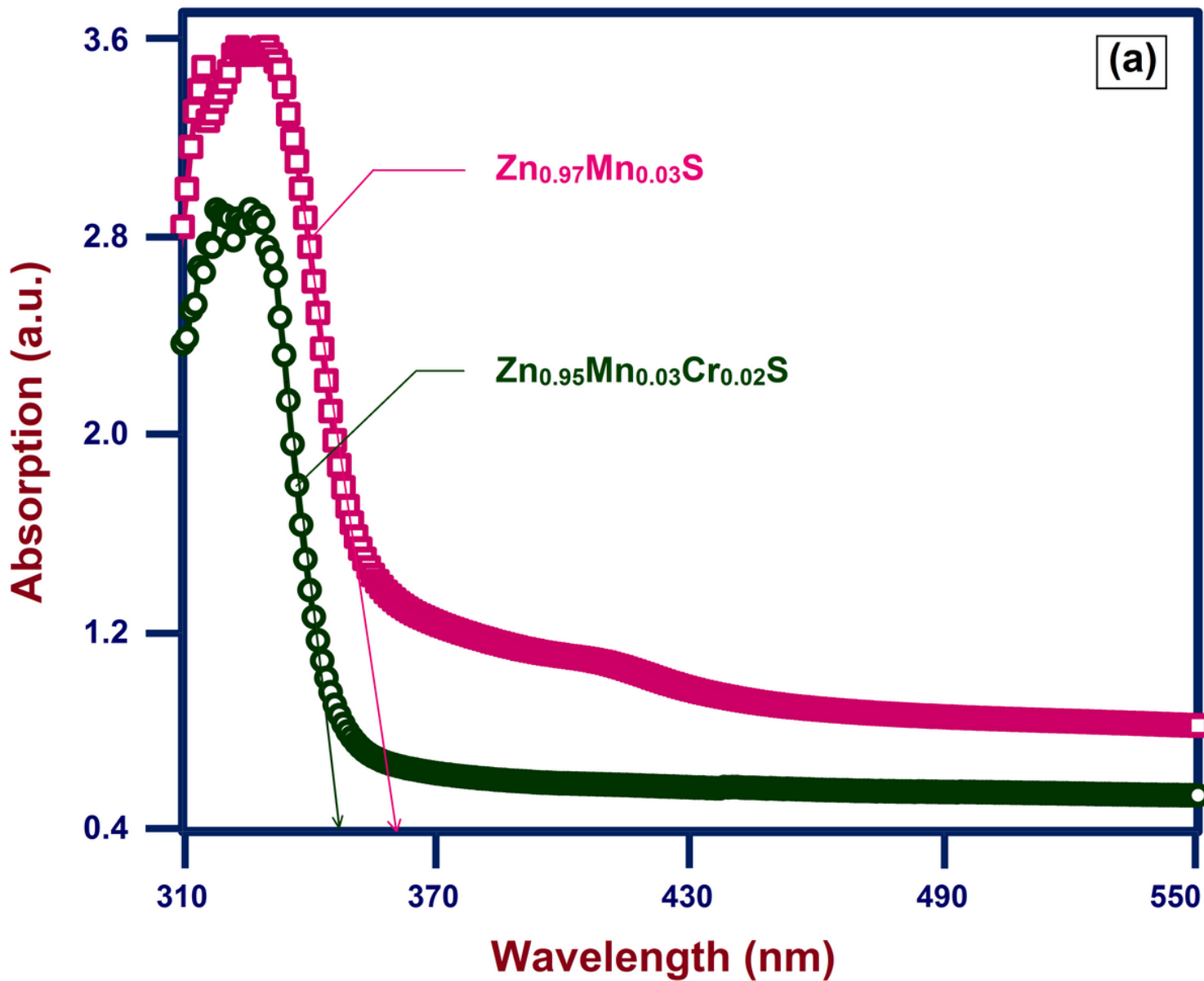


Figure 8

FTIR spectra of $Zn_{0.97}Mn_{0.03}S$ and $Zn_{0.95}Mn_{0.03}Cr_{0.02}S$ nanostructures in the wave number ranging from 400 to 4000 cm^{-1}

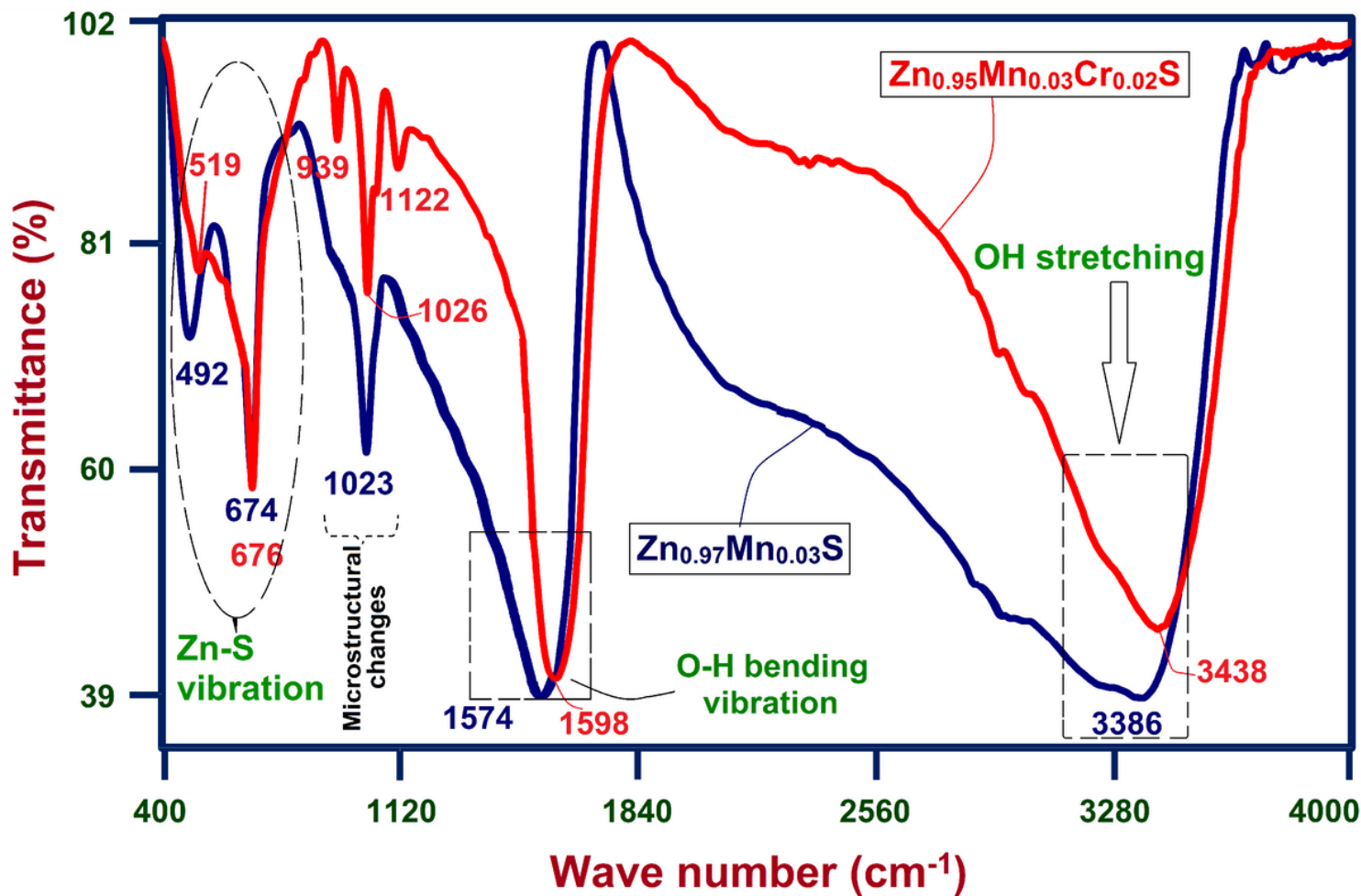


Figure 9

PL spectra of (a) ZnS from 350 to 650 nm, and Zn_{0.97}Mn_{0.03}S and Zn_{0.95}Mn_{0.03}Cr_{0.02}S nanostructures (b) from 345 to 500 nm and (c) from 500 to 700 nm using 330 nm line of Xe excitation source

